Chapter 10
Atomic-Scale Contrast Formation in AFM Images on Molecular Systems

Fabian Schulz, Sampsa Hämäläinen and Peter Liljeroth

Abstract Imaging individual molecules with atomic resolution is now possible using non-contact atomic force microscopy (AFM). In all cases where atomic resolution imaging of molecules was demonstrated, chemically passivated tips were used. This chapter will discuss the factors influencing the atomic scale imaging of molecular systems. We will first discuss the effect of the tip passivation on the atomic scale contrast. Subsequently, we will consider the factors affecting the quantitative details of the apparent atomic positions (background from the neighbouring atoms, flexibility of the tip apex and non-planar samples). Finally, we will discuss how the tip flexibility affects the appearance of the inter- and intramolecular bonds imaged with AFM.

10.1 Introduction

Imaging individual molecules with atomic resolution is now possible using non-contact atomic force microscopy (AFM) in the frequency modulation mode [1]. As discussed in the chapter by Gross and co-workers, such experiments require passivation of the AFM tip apex. In addition to the direct visualization of the molecular structure, AFM has been used to identify different atomic species [2, 3]. Using molecule-terminated tips, it has been shown that the apparent length of chemical bonds in conjugated organic molecules is correlated to the bond order [4] and the intramolecular charge distribution of planar molecules has been mapped [5]. It has even been suggested that intermolecular hydrogen bonding could be imaged using AFM [6]. These new capabilities will allow AFM to be used in chemistry,

F. Schulz · S. Hämäläinen · P. Liljeroth (✉)
Department of Applied Physics, Aalto University School of Science,
PO Box 15100, 00076 Aalto, Finland
e-mail: peter.liljeroth@aalto.fi

F. Schulz
e-mail: fabian.schulz@aalto.fi

S. Hämäläinen
e-mail: sampsa.hamalainen@aalto.fi

molecular electronics, and materials science for structural chemistry at the single-molecule level [7–12].

As mentioned above, in all cases where atomic resolution imaging of molecules was demonstrated, chemically passivated tips were used, typically a carbon monoxide (CO) molecule or a Xe atom adsorbed on the apex [1, 13]. Inert tips are essential to avoid accidental pick-up or lateral manipulation of the molecule of interest by the tip at the small distances and oscillation amplitudes required for atomic resolution imaging. The exact atomic geometry of the tip apex depends on the tip-sample distance, as e.g. the CO is flexible and can bend to reduce the interaction energy between the tip and sample [4, 14–16]. The tip bending can occur both due to attractive and repulsive interactions, i.e. the CO molecule can bend towards or away from the nearest atom. In addition, if the neighboring atoms are not symmetric with respect to the atom directly under the AFM tip, there is a non-symmetric background force on the CO, which will further shift the apparent atomic positions. Finally, the CO bending is sensitive to any saddle points and ridges in the interaction potential energy surface. These will show up as regions of enhanced contrast, irrespective of whether there is an actual bond associated with this region [17, 18].

This chapter will discuss the factors influencing the atomic scale imaging of molecular systems. We will first discuss the effect of the tip passivation on the atomic scale contrast and highlight the complementary nature of the information that can be obtained by AFM and scanning tunneling microscopy (STM). We will then go through the factors affecting the quantitative details of the apparent atomic positions: background forces from the neighboring atoms, flexibility of the tip apex and non-planar samples. Finally, we will discuss the contrast formation mechanism of intra- and intermolecular features in AFM images.

10.2 Tip Reactivity and Atomic Contrast

In non-contact AFM, both the atomic configuration and chemical composition of the tip apex have a profound influence on the imaging contrast at the atomic scale [19–25]. Experiments on model surfaces and with well-defined tip termini are thus crucial in understanding the mechanisms of atomic resolution imaging, which is essential for qualitative and quantitative interpretation of AFM images.

10.2.1 Well-Defined Tips and a Model Surface

The preparation of tips with well-defined apices by picking up single atoms or small organic molecules (commonly referred to as 'tip functionalization') is an established technique within the STM community. Demonstrated for the first time more than 20 years ago [26], different functionalizations may allow for improved spatial resolution [26], chemical contrast [27] or spin sensitivity [28]. The advent of low-amplitude

AFM, in particular through the tuning-fork-based qPlus sensors [29], opened up this experimental approach to the AFM community. Since the qPlus sensor can be easily operated at sub-Å oscillation amplitudes, tunneling current and frequency shift can be measured simultaneously with atomic resolution. This has enabled a straight-forward adaption of tip functionalization schemes developed previously within the STM community.

Arguably the most prominent example is the functionalization of an AFM tip by picking up a single CO molecule, which yields an atomically well-defined AFM tip with a predefined structure, in contrast to the usual case of e.g. silicon tips. The passivating effect of the CO allows to probe the repulsive force regime of individual molecules, leading to breathtaking images of their chemical structure [1]. Reactive metallic tips, in contrast, typically interact too strongly with single molecules, result-ing in lateral or vertical manipulation before the tip-sample distance is sufficiently small for atomic resolution imaging. Thus, to understand how the reactivity of the tip affects the atomic contrast in organic molecular systems, a mechanically stable model surface is required. A convenient choice is an epitaxial graphene monolayer on a metal surface, as the structure of graphene resembles the carbon backbone of organic molecules. Due to the attractive van der Waals (vdW) interaction with a metallic substrate, epitaxial graphene constitutes a mechanically stable surface that can be imaged with reactive and non-reactive tips.

Graphene possesses a very simple structure, made of a single atom thin layer of car-bon atoms arranged in a honeycomb lattice, as shown in Fig. 10.1a. This honeycomb structure gives rise to exciting electronic properties in graphene [30, 31], in particular a linear dispersion in the band structure around the Fermi level and a large charge carrier mobility. As a result, graphene holds great promise in electronic applications. At the same time, it continues to be the topic of intense basic physics research as it can host exotic electronic phenomena such as Klein tunnelling, integer and fractional quantum Hall effects, and weak localization [31]. These reasons have resulted in a strong drive to characterize graphene in detail both experimentally and theoretically, making it a well-understood model system.

Among the epitaxial systems, graphene on Ir(111) [G/Ir(111)] has attracted the largest interest, as the graphene can be grown on iridium with high quality [32] by simple chemical vapour deposition (CVD) using small hydrocarbon molecules such as ethylene. In addition, the interaction with the Ir(111) surface is sufficiently weak such that basic electronic properties of the graphene, e.g. the linear dispersion in the band structure, are preserved [33].

G/Ir(111) thus constitutes the desired model surface to study how tip reac-tivity affects the imaging contrast in AFM. Atomically resolved force-distance spectroscopy and constant-height images of the epitaxial graphene layer reveal that reactive and non-reactive tips exhibit comparable atomic contrast at short tip-sample distances at the onset of Pauli repulsion, while there are striking disparities in the attractive force regime at medium tip-sample distances [24].
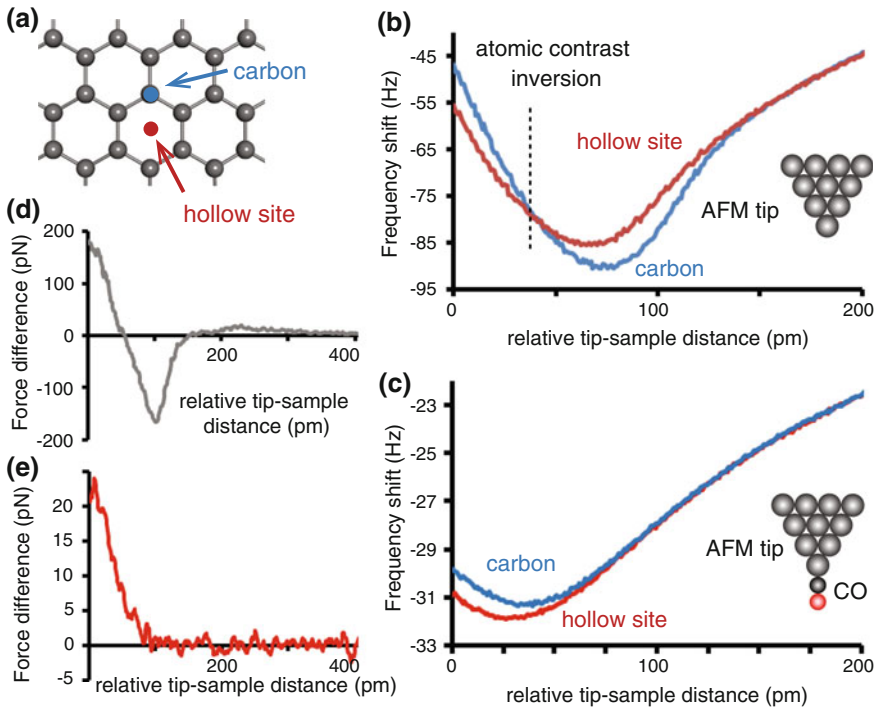
Fig. 10.1 Force spectroscopy on graphene on Ir(111). **a** The carbon honeycomb lattice of graphene. **b** Frequency shift as a function of tip-sample distance for a carbon and a hollow site, measured with a reactive Ir tip. **c** Same as (**b**) but with a non-reactive CO tip. **d** Difference of the measured short-range forces between the carbon atom and the hollow site for the reactive tip. **e** Same as (**d**) but for the non-reactive tip. Adapted with permission from [24]. Copyright (2012) American Chemical Society

10.2.2 Force Spectroscopy with Reactive and Non-Reactive Tips on Epitaxial Graphene

A reactive metallic tip can be prepared by deliberate, microscopic contact formation of the tip with a clean metal substrate, resulting in the pick-up of surface atoms. In the case of AFM measurements on G/Ir(111), this leads to an Ir-terminated tip apex. As iridium is a transition metal with a partially filled 5d shell, the Ir tip constitutes a reactive apex that will readily interact with the sample.

The tip-sample interaction can be quantified by measuring the frequency shift (Δf) of the tuning fork as a function of the tip-sample distance (d_{ts}). This is demonstrated in Fig. 10.1 on two characteristic sites of the graphene honeycomb lattice: on top of a carbon atom and in between them on a hollow site (marked in Fig. 10.1a). Both $\Delta f(d_{ts})$ curves are displayed in Fig. 10.1b. At large tip-sample distances, the two curves overlap, since long-range vdW forces between the macroscopic body

of the tip and the sample—with negligible site-specific contributions—dominate. However, as the tip approaches the graphene, short-range forces between the tip apex and the carbon lattice come into play and the two $\Delta f(d_{ts})$ spectra start to deviate: first, at medium distances, the Δf measured over the carbon atom reaches significantly larger negative values compared to the hollow site. Approaching the tip further beyond the minimum Δf sees this trend reversing until the two curves cross. Now, at short tip-sample distances, the carbon atom shows a less negative Δf than the hollow site.

The reactive iridium tip can be passivated by picking up a single CO molecule, yielding a non-reactive tip apex due to the closed-shell character of the CO. The procedure has been demonstrated on weakly reactive metal surfaces such as Cu(111) and Au(111), but it is very difficult to controllably pick up CO from more reactive substrates such as the Ir(111) surface. There are two alternative procedures that can be followed. In the first one, the tip can be prepared on a Cu(111) surface, where the CO pick-up is well-documented. Subsequently, the Cu(111) is exchanged with the desired substrate, in this case the graphene-covered Ir(111) sample and the experiments are carried out. The presence of the CO on the tip can be confirmed afterwards by going back to a Cu(111) substrate and checking the image contrast over a CO adsorbed on the surface in STM feedback. If the images are taken with a CO-terminated tip, CO on Cu(111) has a characteristic sombrero-like appearance [27]. Imaged with a metal tip, it appears as a depression.

The tip termination can also be checked on the G/Ir(111) surface by taking advantage of the moiré superstructure formed by graphene on Ir(111). The lattice mismatch between the graphene and the iridium surface causes a periodic modulation of the atomic registry and adsorption height of the carbon atoms w.r.t. the iridium substrate. Thus, the graphene buckles and forms a periodic pattern of hills and valleys (the moiré pattern) [34]. Typically, with a metal tip the contrast of the graphene moiré is inverted in low-bias STM images. This changes with a CO on the tip apex and the moiré contrast corresponds to the true topography in low-bias STM images. This enables a second procedure to prepare a CO tip, directly on the G/Ir(111) sample without exchanging for a Cu(111) surface. A small amount of CO can be dosed directly into the cryostat and scanner at low temperature, which will lead to the adsorption of a CO molecule on the tip apex in a stochastic process [35].

Having prepared a CO-terminated tip, an equivalent set of measurements is performed (shown in Fig. 10.1c) as was done using the iridium tip. Similarly to the Ir tip, the $\Delta f(d_{ts})$ spectra of the non-reactive CO tip measured over the carbon atom and over the hollow site overlap at large tip-sample distances. At these distances, the tip-reactivity does not play a role as long-range forces dominate and short-range forces between the tip apex and the sample can be neglected. In contrast to the Ir tip, the two curves measured with the CO tip continue to overlap at medium distances as the tip approaches the sample. Only as the tip reaches the Δf minimum and approaches the graphene layer further, the spectra for the carbon atom and the hollow site start to deviate from each other, with the carbon atom exhibiting a less negative Δf, similar to the case of the reactive Ir tip at short distances.

Figure 10.1d, e highlight the differences in the measured tip-sample forces between the two tips: for each tip, the $\Delta f(d_{ts})$ spectrum on the hollow site was subtracted from the spectrum measured over the carbon atom to remove the uniform background due to the long-range van der Waals forces. Subsequently, the difference spectra were converted into force-distance $[\Delta F(d_{ts})]$ curves using the Sader-Jarvis formula [36]. Thus, the $\Delta F(d_{ts})$ curves reveal the force between the carbon atom in the graphene lattice and the very apex of the tip (Ir or CO), responsible for the atomic contrast. The reactive Ir tip (Fig. 10.1d) yields considerable differences in the tip-sample forces, both in the attractive and repulsive regime, over a total distance range of 150 pm. Thereby, the maximum attractive force over the carbon atom is 150 pN larger than over the hollow site, in agreement with density functional theory (DFT) predicting the preferred adsorption of Ir atoms on top of the carbon atoms [37]. The passivated CO tip (Fig. 10.1e), on the other hand, does not show any appreciable difference in the attractive force regime between the carbon atom and the hollow site. Only within a narrow region of short tip-sample distances, at the onset of Pauli repulsion, the forces over the two inequivalent lattice sites differ, with the carbon atom being approximately 25 pN more repulsive than the hollow site.

The observed behaviour is in good agreement with DFT calculations of the force between different tips and either graphene or a carbon nanotube [21]. A reactive tip was predicted to cause a re-hybridization of the carbon atoms, resulting in strong short-range attractive forces which are maximal at the carbon lattice site. At closer distances, the larger electron density at the carbon atoms lead to stronger Pauli repulsion and thus, the hollow sites appear with larger attractive force, effectively reversing the atomic contrast. For non-reactive tips, the attractive short-range forces are very small, and atomic contrast between carbon and hollow sites is reached only in the regime of Pauli repulsion, where the differences in electron density yield the same contrast as for reactive tips.

10.2.3 (Non-)Reactivity Determines the Imaging Contrast

The force-distance characteristics between tip and sample will ultimately determine the atomic contrast that is achievable in AFM images. Thus, constant-height images of the Δf signal recorded over the graphene layer, as shown in Fig. 10.2, can be easily interpreted when considering the $\Delta f(d_{ts})$ spectra.

For the reactive Ir tip (Fig. 10.2a, b), two different atomic contrasts can be observed: at larger tip-sample distances ($z = 60$ pm), a hexagonal pattern of local Δf maxima (i.e. less negative Δf) appears, indicating the positions of the less attractive hollow sites. This contrast reverses at short distances ($z = 0$ pm), where the increased Pauli repulsion at the carbon atoms due to the larger electron density results in a honeycomb lattice of less negative Δf.

The additional long-range superstructure visible in the images marks the hills and valleys of the G/Ir(111) moiré pattern. The buckling of the graphene layer allows the observation of both kinds of atomic contrast simultaneously at intermediate
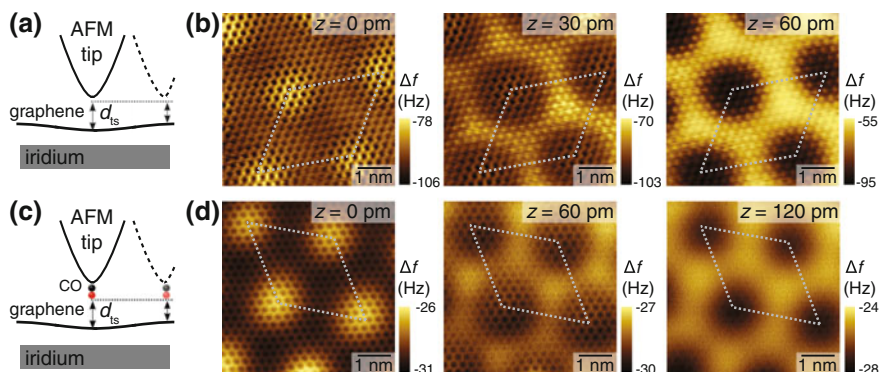
Fig. 10.2 Constant-height images of epitaxial graphene. **a** Schematic of the Ir tip scanning over the G/Ir(111) moiré pattern, which modulates the tip-sample distance. **b** Series of Δf images for increasing tip-sample distance from *left* to *right* (relative tip height indicated on the panels). **c**, **d** Same as (**a**) and (**b**) but for the CO tip. Adapted with permission from [24]. Copyright (2012) American Chemical Society

tip-sample distances ($z = 30$ pm). In this intermediate regime, the tip apex already feels Pauli repulsion on the moiré hills, imaging the carbon lattice with less negative Δf, while on the valleys the atomic contrast is still governed by short-ranged attractive forces and the hollow sites appear with less negative Δf. (Notice that the overall forces are still attractive, as the hills are imaged with larger negative frequency shift than the valleys, while the Pauli forces between the carbon atoms and the tip only cause an additional repulsive modulation on top of the attractive background on the hills.) This proves that both contrasts are characteristic for reactive tips, and the tip-sample distance determines which one is observed.

In accordance with the spectra in Fig. 10.1, the images recorded with a CO tip (Fig. 10.2c, d) do not show atomic contrast in the attractive regime ($z = 120$ pm). Only the long-range periodicity of the moiré pattern is visible, with the hills being imaged with larger negative Δf. At intermediate distances ($z = 60$ pm), the repulsive contrast displaying the honeycomb lattice starts to appear as a modulation of the overall attractive contrast. Finally, the repulsive contrast is observed on the entire graphene surface at short tip-sample distances ($z = 0$ pm), similarly to the reactive tip.

10.3 Relating Electronic Properties with Atomic Structure

As the size of electronic devices continues to shrink, the exact atomic scale structure of the active device area, including the position of individual defects or dopant atoms becomes relevant for the device function. This requires the development of techniques that can simultaneously yield atomic scale structural and electronic information.

AFM based on the qPlus tuning fork design achieves this aim as the small oscillation amplitudes make it possible to carry out simultaneous STM experiments with uncompromised quality [9, 10, 12, 38, 39].

There is intensive research trying to replace silicon transistors with devices where the active element is a single atom or a molecule. Therefore, measurements of structural and electronic properties of such nanostructures are becoming increasingly important. Since their electronic properties are correlated to their precise atomic arrangement and composition, already zero-dimensional defects (also referred to as point defects, e.g. a single missing or substituted atom) can significantly change the electronic structure of such molecular systems, eventually hampering their intended functionality. This is in particular true for many transport properties determined by delocalized electrons, for which defects act as strong scattering potentials [40]. Identifying defects at the atomic scale is thus crucial to understand their effect on the electronic properties, and to develop strategies minimizing their occurrence.

10.3.1 AFM Versus STM and Finite-Size Effects in Graphene

Scanning tunneling microscopy appears as a natural choice to examine atomic scale defects. However, STM measures the local density of states (LDOS) of a sample, and it is doing so only in a narrow energy range around the Fermi energy, being most sensitive to the highest occupied and lowest unoccupied states. In conjugated molecular systems, these states usually host delocalized electrons, whose wave functions can be spread out over the entire backbone of the molecule, while exhibiting a complex structure of lobes and nodal planes. The LDOS of such states does not allow a straight-forward reconstruction of the actual chemical structure of the molecule, as demonstrated in Fig. 10.3a. The presence of defects further complicates the issue, as they act as scattering centers for these delocalized electrons [40], resulting in additional deformations of their wave functions. Identification of the atomic structure of defects by STM is possible only by means of extensive ab initio electronic structure calculations for a set of possible defect structures and subsequent comparison with the experimentally measured wave functions [42].

As has been discussed in the other chapters of this book, AFM is sensitive to the total electron density when probing the repulsive force regime [5], as the strength of Pauli repulsion scales with electron density. Since the total electron density is dominated by core electrons localized at the positions of the atomic nuclei, an AFM image taken in the repulsive regime gives direct information on the atomic structure of the sample. Intensity differences in the sub-molecular contrast can be related to variations in the total electron density, caused by the chemical composition of the molecule or deformations of its structure. Thus, AFM should provide a superior tool to identify the atomic structure and defects in molecular systems.

We illustrate this below using graphene nanoribbons (GNR) synthesized through on-surface polymerization as examples [38, 43]. These graphene nanostructures allow the tuning of the electronic properties through finite-size effects. Infinite
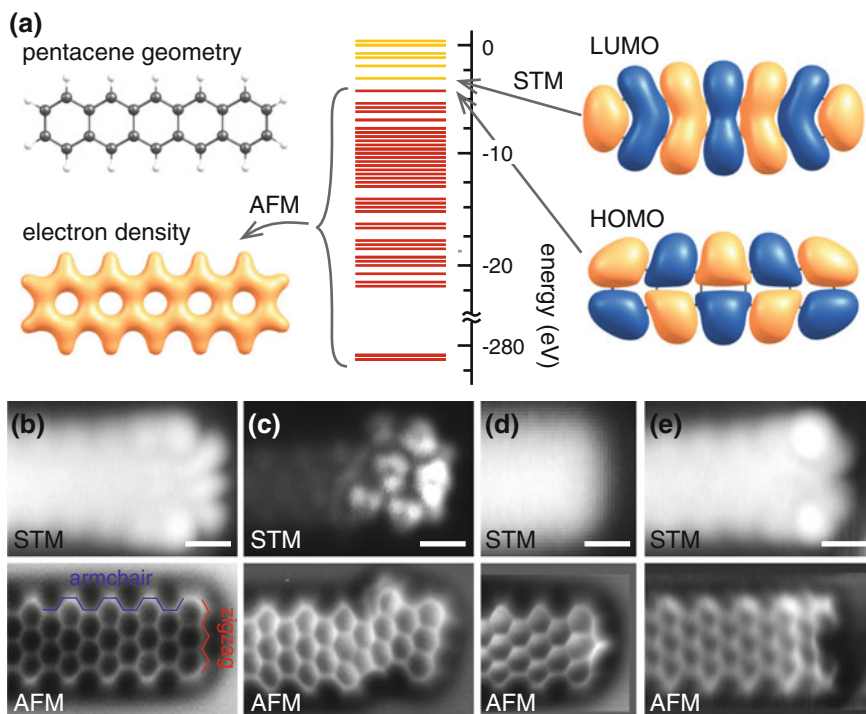
Fig. 10.3 Atomic structure of defects in graphene nanoribbons. **a** Schematic highlighting the different origins of imaging contrast in STM and AFM. STM images molecular orbitals close to the Fermi level (e.g. highest occupied molecular orbital, HOMO and lowest unoccupied molecular orbital, LUMO), while AFM images the total electron density dominated by localized core electrons. **b**–**e** Constant-current STM (*upper panel*) and constant-height AFM (*lower panel*) of (**b**) a defect free GNR exhibiting an edge state at the zigzag (ZZ) edge, but not at the armchair (AC) edge, (**c**) a tilted GNR, (**d**) a GNR with one ZZ edge C atom passivated by two H atoms and (**e**) a GNR with one ZZ edge C atom bonding to the Au(111) substrate. All scale bars are 5 Å. Panels **b**, **d**, and **e** adapted with permission from [38]. Panel **c** adapted with permission from [41]. Copyright (2013) by the American Physical Society

graphene sheets are characterized as semi-metallic or zero-gap semiconductors, due to the crossing of the π bands at the Fermi energy with zero density of states [30]. Quantum confinement effects can open a gap in the band structure in finite graphene flakes of suitable dimensions [44]. In addition, the zigzag (ZZ) edges of graphene (Fig. 10.3b), representing the 'cutting' of graphene along one of its high-symmetry directions, host a non-dispersive electronic edge state at the Fermi energy [31]. This state is neither present in infinite graphene nor on other edge structures [e.g. armchair edges (Fig. 10.3b)]. The interest in graphene zigzag edges stems from the predicted phenomena that would allow the construction of new types of electronic devices (based on e.g. spintronics or valleytronics) [45, 46].

Atomically well-defined GNRs which host edge states can be synthesized on metallic surfaces using molecular precursors [43]. The synthesis is carried out by evaporating the desired precursor onto the substrate [e.g. Au(111)], followed by thermally induced polymerization and cyclodehydrogenation to eventually form the GNR. The beauty of this approach is that the structure of the GNR is uniquely determined by the precursor and this allows for example the width of the GNR to be controlled precisely. The electronic structure of these GNRs is sensitive to chemical modifications of graphene and its edges, and correlating atomic geometry with the electronic structure is an important issue for potential applications [38].

10.3.2 Imaging Defects in Graphene Nanoribbons

Figure 10.3b shows the Δf signal recorded with a CO-passivated tip at constant height over a defect-free GNR. Recorded in the repulsive force regime, the image can be directly interpreted in terms of the atomic structure of the GNR, revealing long edges with armchair (AC, blue) symmetry and a short ZZ edge (red). The corresponding STM image (metallic tip) displays the LDOS of the ZZ edge state, in agreement with simulations (not shown) [38]. The STM image of a different GNR in Fig. 10.3c (CO tip), on the other hand, suggests a deviation at the ribbon termination from the otherwise perfectly straight structure. While a slight tilting at the end of the GNR is already noticeable in the STM image, it does not allow to identify the exact atomic arrangement that causes this tilt. Only the AFM image (Fig. 10.3c), showing the carbon backbone, reveals the origin of the tilt as the displacement of the terminating segment by one graphene lattice vector in combination with the formation of a carbon pentagon [41].

Even more subtle effects such as chemical modifications can be identified in this manner. Figure 10.3d shows the STM image of a GNR ZZ termination displaying no end state. Such contrast was previously assigned to a missing carbon atom [47], destroying the symmetry of the ZZ edge and thereby causing the disappearance of the edge state. However, the corresponding AFM image presented in the same panel unambiguously proves that the carbon backbone is still intact. On the contrary, an increased intensity (i.e. increased repulsion) on the central outermost carbon indicates additional electron density, interpreted as the passivation of the C atom by two hydrogens instead of just one. The corresponding change from sp^2 to sp^3 hybridization would destroy the edge state. It can be recovered by applying a bias voltage pulse with the SPM tip to remove the extra hydrogen atom. Applying a second bias pulse results in a further modification of the GNR edge, as testified by the STM image in Fig. 10.3e. This image, recorded after applying a voltage pulse to an unmodified, defect-free GNR ZZ edge, still resembles that of the ZZ edge state, but the intensity distribution has changed remarkably. The corresponding AFM image shows strongly reduced repulsion at the central outer C atom. An image taken at a smaller tip-sample distance (not shown) reveals an intact carbon backbone, indicating that the GNR edge bends down towards the substrate [38]. This suggests

that the bias pulse removed the single H atom at the central outer C atom, which subsequently formed a bond with the underlying Au(111). This would preserve the sp^2 hybridization of the edge atoms and thus the edge state, while explaining the observed change in the intensity distribution of its wave function.

These experiments highlight the type of complimentary information that can be obtained through combined STM and AFM experiments. These are clearly extremely important for the detailed understanding of the correspondence between the atomic scale structure and the resulting electronic properties of atomically well-defined nanostructures.

## 10.4 Understanding Measurements with a Flexible Tip Apex

In the preceding sections, we have treated the effects of the tip termination on the observed AFM response and shown how STM and AFM can yield complimentary information on molecules and nanostructures. We will now move on and focus on the quantitative details of AFM imaging with molecule-terminated tips.

10.4.1 Measuring Interaction Energies with a Molecule-Terminated Tip

What is actually measured in an AFM experiment with a molecule-modified tip? It turns out that the tip relaxation has to, in general, be considered for a detailed understanding of the measured forces [4, 9, 14–16]. This process is illustrated in Fig. 10.4, where the relevant interaction terms have been indicated for the measurements of the background signal (Fig. 10.4a) and on the molecule (Fig. 10.4b). The figure and the following discussion consider a CO-terminated tip as an example, but the general principle is naturally applicable to understanding any experiment with a flexible tip apex.

When the tip interacts with the bare substrate, the interaction potential can be formally divided into three terms: the interaction between the body of the tip and

Fig. 10.4 Division of the total interaction energy between a CO-terminated AFM tip and a clean substrate (**a**) and a substrate with an adsorbed molecule (**b**)
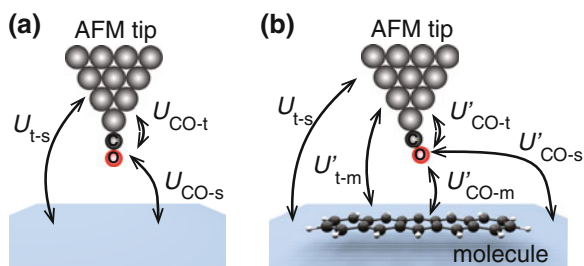
the substrate U_{t-s} and the interaction energies between the CO molecule and the substrate U_{CO-s} and the tip U_{CO-t}, respectively. The situation changes when the tip is brought above a molecule adsorbed on the surface. We have new interaction terms between the body of the tip and the molecule U'_{t-m} and between the CO and the adsorbed molecule U'_{CO-m}. In addition, if the interaction between the CO on the tip with the molecule is sufficiently strong, this will cause the CO molecule to bend. This bending causes interaction energies U'_{CO-s} and U'_{CO-t} to change compared to the experiments on the clean surface. The total interaction energy can now be written (for a given tip height)

$$\Delta U = U'_{t-m} + \left(U'_{CO-t} - U_{CO-t}\right) + \left(U'_{CO-s} - U_{CO-s}\right) + U'_{CO-m} \qquad (10.1)$$

where the terms U_{t-s} cancel. In terms of measuring interactions between molecules, or for the sake of simple modelling of the AFM response, it would be desirable to be able to measure only the interaction energy U'_{CO-m}. If the CO molecule on the tip does not relax, then the terms in the parenthesis in (10.1) cancel. The term U'_{t-m} can in principle be obtained from a measurement on a molecule before tip functionalization. In that case, it is possible to derive the interaction potential between the CO on the tip and the molecule adsorbed on the substrate purely based on experiments. However, if the CO on the tip relaxes, the terms in the parenthesis are non-zero and there is no direct experimental access to the term U'_{CO-m}. Finally, the above treatment does not take into account the possible relaxation of the molecule on the surface which would further complicate the analysis [14].

10.4.2 Can Atomic Positions Be Measured Quantitatively by AFM with Molecule-Terminated Tips?

In order to understand the atomic-scale imaging mechanism with molecule-terminated tips, it is very helpful to construct a simple model of the tip-sample junction. We have used an approach based on molecular mechanics and pairwise Lennard-Jones (L-J) potentials, where the main tunable parameter is the lateral spring constant k_{CO} of the CO molecule on the tip. While this model is much more simplistic than DFT-based calculations, the major advantage of the present model is that we can freely vary k_{CO} and therefore systematically study the effect of the tip flexibility. In DFT calculations, this number is fixed by the choice of the metal cluster used as a tip model. Details of the model can be found in [15, 18].

   We will first consider a well-studied model system to understand in detail the various background contributions to the measured AFM response. For this, we use a pentacene molecule adsorbed directly on a metal (Fig. 10.5) [1, 15]. Simulated constant-height Δf maps with two different lateral spring constants k_{CO} are shown in Fig. 10.5a. It is immediately obvious that both strongly resemble experimental AFM images of pentacene (see chapter by Gross et al.). The simulations are able to
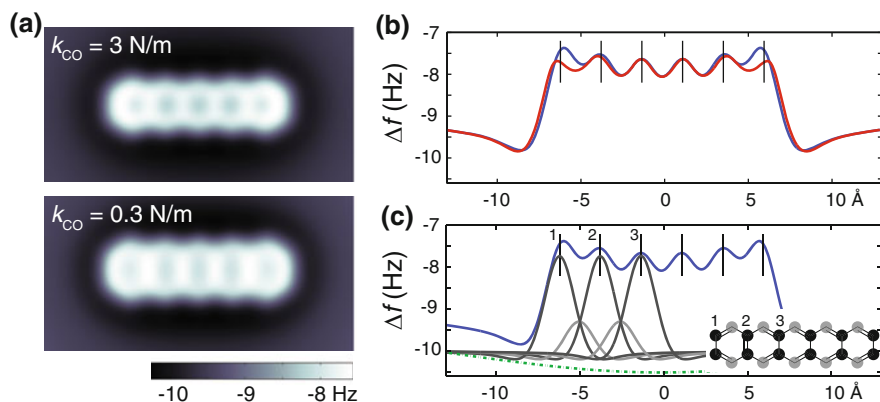
Fig. 10.5 a Simulated constant-height AFM images of pentacene with a relatively stiff ($k_{CO} = 3$ N/m) and soft ($k_{CO} = 0.3$ N/m) CO lateral force constant. **b** Extracted line profiles along the center of the pentacene molecule for the two tips (*blue line* corresponds to $k_{CO} = 3$ N/m and *red line* to $k_{CO} = 0.3$ N/m). **c** Line profile over the center of the pentacene molecule for a rigid tip, which also shows the contributions from the individual dimers (*black and gray lines*, the corresponding atoms are indicated in the *inset*) and the overall van der Waals background between the CO molecule and the pentacene (*green dotted line*). Adapted with permission from [15]. Copyright (2014) American Chemical Society

reproduce the three main effects where the experimental Δf map differs from the actual structure of the pentacene molecule: (i) all the phenyl rings are elongated in the y-direction; (ii) the edgemost phenyl rings are also elongated in the x-direction; (iii) as the tip-sample distance is reduced, the bonds appear sharper (as discussed in more detail in Sect. 10.4.4) [4, 15–17].

To identify the origin of these effects, we start by extracting the positions of the CO at the end of the tip during each step of the simulation. It shows that the CO bends in response to the tip-sample interaction. The overall bending at the outer edge of the molecule is always towards the center of the molecule and is caused by the attractive van der Waals interaction between the CO molecule and the pentacene. When the tip is over the molecule, it can bend away from the nearest atom at sufficiently small tip-sample distances, irrespective of the vdW background. The maximum CO displacement is of the order of a couple of pm for the stiffer tip, but can reach several tens of pm for the softer tip. This naturally depends on the tip-sample distance.

In addition to the tip bending, the background forces from the neighboring atoms also affect the apparent atomic positions. Figure 10.5b shows Δf line profiles along the center of the pentacene molecule for a flexible ($k_{CO} = 0.3$ N/m, red line) and a stiff ($k_{CO} = 3$ N/m, blue line) tip. The peaks in the Δf line profiles correspond to the apparent positions of the carbon dimers along the middle of the pentacene molecule. Their real, geometric, positions are marked by vertical lines. Finally, Fig. 10.5c gives the contributions from the individual dimers (black solid lines), and the outer most carbon atoms (gray lines, see inset for a schematic) for a rigid tip ($k_{CO} \to \infty$). The

green dotted line gives the overall vdW attraction between the bulk Ir tip and the pentacene molecule.

From Fig. 10.5c it is immediately obvious that the peaks corresponding to the left- and rightmost carbon atoms are shifted significantly towards the center of the molecule (lateral shift of ca. 25 pm). This is due to the asymmetric background signal from the neighboring atoms. All the neighboring atoms contribute to the measured Δf signal, and since the last dimer of the pentacene has neighboring atoms only on one side, this causes an apparent shift in the position of the C–C bond. Contrary to outer dimer 1 being shifted towards the right, the peak corresponding to dimer 2 is shifted towards the left, i.e. the outermost benzene ring appears contracted on both sides. This small shift (around 5 pm depending on the tip height) is due to the slope of the vdW background between the tip and the whole pentacene molecule. While this effect is also also present on the last dimer, the asymmetry in the neighboring atoms has the dominant contribution there. In planar molecules, these effects will always cause an apparent contraction towards the center of the molecule of the outermost rings.

Comparison between the simulations with a rigid ($k_{CO} = 3$ N/m, blue line) and a soft ($k_{CO} = 0.3$ N/m, red line) CO tip shown in Fig. 10.5b allow the assessment of the tip flexibility on the apparent atomic positions. The results obtained with the stiffer tip are quantitatively very close to the rigid tip discussed in Fig. 10.5c. As k_{CO} becomes smaller, the bending of the CO increases. In general, the van der Waals attraction causes the molecule at the tip to bend towards the center of the pentacene. As a result, the outermost bonds appear stretched, both in x- and y-directions. Hence, the effect of tip flexibility is opposite to that of the asymmetric background forces. The dominant contribution depends on k_{CO} and the tip-sample distance.

10.4.3 Can AFM Images Be Background Corrected on the Atomic Scale?

The previous section described how neighbouring atoms affect the measured AFM response and the positions of the Δf maxima corresponding to the atoms. In the general case, it is also possible that the atoms are on different heights, if the molecule or the surface has a three-dimensional shape. We will investigate this on the previously introduced model system of an epitaxial graphene monolayer grown on the Ir(111) surface. According to both experimental and theoretical work [15, 16, 48], AFM in either the constant-height or constant-frequency shift mode will detect apparent lateral changes in the atomic positions on corrugated surfaces. Typically, most of the apparent shift in the atomic position is caused by the asymmetric background from the neighboring atoms that are at different adsorption heights. This suggests that an appropriate background correction or subtraction could be used to correct the experimental data and allow us to extract the actual atomic structure and positions from the experiments. This idea can be tested using the simulated images of graphene on
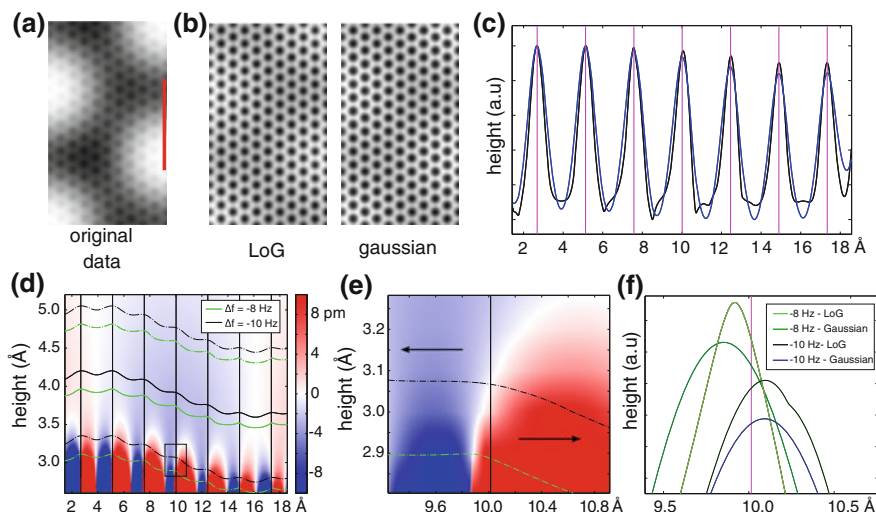
Fig. 10.6 **a** Simulated constant-Δf AFM image of the graphene moiré on Ir(111) with a stiff tip ($k_{CO} = 3$ N/m). **b** Background subtracted images using either a Laplacian of Gaussians filter ($\sigma = 0.6$ Å) or a heavily Gaussian blurred background ($\sigma = 1$ Å). **c** Normalized cross sections of the image in panel a along the *red line* (*blue line* with Gaussian background, *black line* with LoG). The *vertical lines* mark the positions of the bonds. **d** Cross section along the *same line* for a more flexible tip ($k_{CO} = 0.6$ N/m) calculated with two different Δf set points. The *solid lines* correspond to the tip height, while the *dotted lines* show the limits of the oscillation amplitude. The *background color* corresponds to the bending of the CO along the same section. **e** Close-up of the bending in the area marked in panel (**d**). **f** The background corrected cross sections of the same bond. Adapted with permission from [15]. Copyright (2014) American Chemical Society

Ir(111), of which the results are summarized in Fig. 10.6. The simulated constant-Δf image in Fig. 10.6a shows strong long-range corrugation due to the G/Ir(111) moiré pattern, and examples for different background corrections are shown in Fig. 10.6b. In principle, the moiré corrugation can be removed from the simulated images using different filtering schemes. Here, the background was removed either with a Laplacian of Gaussians (LoG) filter, which reduces the contributions from slowly varying long-range corrugations or through estimating the background by heavily blurring the original images by a Gaussian filter and subtracting this from the original image. Line profiles along the segment indicated by a red line in Fig. 10.6a with the two filtering schemes are shown in Fig. 10.6c.

As can be seen in the line scans, background subtraction of the AFM image results in an apparent expansion of the graphene hexagons on the hills of the moiré pattern, which is the reverse trend compared to that in the non-corrected data (not shown in Fig. 10.6) [15]. Background correction improves the match between the apparent and real bond positions in both the constant-frequency shift and constant-height images. The apparent positions in background corrected data can be as close as 1 pm from the real bond positions; however, typically the difference is of the order of 3–5 pm.

While these differences depend on the exact form of the background, the tip-sample distance, the lateral force constant of the tip etc., it appears that using the Gaussian blurred image as the background in constant-frequency shift images results in very accurate estimation of the bond positions to within <2 pm.

As discussed above, the effects of the unequal background from the neighboring atoms can be significantly reduced by the background correction in the case of a stiff tip. What is the situation with a more flexible tip apex? We show simulated line scans with a softer tip ($k_{CO} = 0.6$ N/m) in Fig. 10.6d with two different Δf setpoints (-8 and -10 Hz on the repulsive branch). The main difference between these setpoints is that at $\Delta f = -8$ Hz, the CO reaches the region where it starts to bend away from the top sites (red background) at the bottom of its oscillation cycle. On the other hand in the $\Delta f = -10$ Hz image, the CO remains bent towards the hill of the graphene moiré over the full oscillation cycle. This is shown in the zoomed-in image in Fig. 10.6e. Figure 10.6f shows the same zoom-in after background correction with the two methods described above. In the case of the $\Delta f = -8$ Hz image, the apparent bonds are closer to the hill of the graphene moiré, while for the case $\Delta f = -10$ Hz, they are farther from it. This is in line with the tip bending away and towards the hill of the graphene moiré, respectively. In addition, the flexibility of the CO causes the bonds to appear sharper at the shorter tip-sample distance. This bond sharpening also has a slight effect on the apparent bond positions after background subtraction. Hence, the shift in Fig. 10.6f cannot fully be attributed to the tip bending. However, the shift in Fig. 10.6f is ca. 20 pm, which is larger than the typical shifts due to changes in the peak shape.

10.4.4 AFM Contrast on Intra- and Intermolecular Bonds

The discussion on how bonds and atoms in AFM images get distorted due to the flexibility of the tip apex begs the question of what we are exactly imaging on top of the bonds, i.e. do we really see the bond? As is discussed in the chapter by Gross et al., the repulsive force in AFM is related to the overlap of the electron clouds of the tip apex and the sample [1, 49]. Curiously, images of molecules taken with functionalized tips often exhibit much sharper contrast between atoms than would be expected by just considering the total electron density of the sample [4, 17, 18].

This sharp contrast arises from the flexibility of the tip apex. The basic mechanism can be understood by considering the same simple molecular mechanics tip model presented in the previous section and applying it to two carbon atoms sitting on a surface as shown in Fig. 10.7. The simulated AFM response with a rigid CO on the tip apex, shown in Fig. 10.7a, displays two overlapping spheres, as one would expect for the spherically symmetric L-J interactions used in the model.

Letting the CO relax due to the tip-sample interaction changes the response considerably and a sharp line appears between the atoms (Fig. 10.7b). This sharpening can be related to how the CO bends in the repulsive potential on top of the atoms. The contours in Fig. 10.7c represent the potential felt by the oxygen atom of the CO
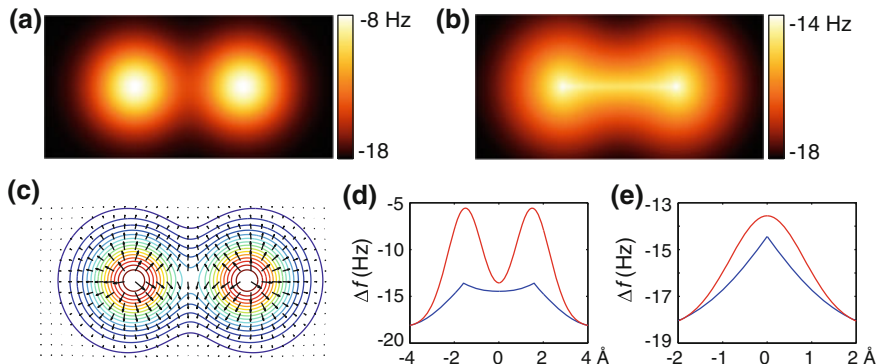
Fig. 10.7 Comparison of contrast in constant-height AFM images on top of two carbon atoms simulated using a tip with a rigid (**a**) and a flexible (**b**) CO apex ($k_{CO} = 0.6$ N/m). **c** Contour of the potential of the oxygen atom on the CO above the two atoms with the quiver plot showing the direction of the CO displacement in the potential. **d** and **e** Cross-sections along and across the apparent bond, respectively. Adapted with permission from [18]. Copyright (2014) by the American Physical Society

on top of the two atoms. As the CO on the tip apex is flexible, it bends away from the atoms at sufficiently small tip-sample distances (quiver plot on top of potential in Fig. 10.7c). The steeper the lateral gradient of the potential, the more the tip bends. In addition to relieving the lateral forces on the tip apex, the bending of the CO also decreases the vertical force, hence affecting the frequency shift.

The curvature of the potential energy defines how the vertical force map is affected. On a convex part of the potential ($\partial^2 U/\partial x^2 < 0$ or $\partial^2 U/\partial y^2 < 0$), the lateral force increases the more the tip bends. This leads to the sharpening of the potential maxima in the force map. On the other hand, a concave potential ($\partial^2 U/\partial x^2 > 0$ or $\partial^2 U/\partial y^2 > 0$) will cause the tip to bend less the farther the tip is moved from the maxima, leading to a flattening of the repulsive region in the force map. This rule of thumb can be applied independently along different coordinate directions. When the tip is scanned well above the plane of the atoms, it feels locally convex potentials centered at the positions of the atoms (assuming the tip is still close enough to reach the repulsive regime). However, the sum of the potentials produces a saddle surface on the line between the atoms. Following the above arguments, F_z is leveled along the saddle surface (concave), but sharpened perpendicular to it (convex). This is evident by comparing the cross sections of the Δf signal along (Fig. 10.7d) and across (Fig. 10.7e) the saddle surface between the atoms.

An interesting feature in the simulated images is that the intensity of the Δf signal decreases the most due to the tip flexibility directly on top of the atoms. In order to understand this, it is useful to directly look at the gradient of the vertical component of the force $\partial F_z/\partial z$. The simulated images in Fig. 10.7a, b take into account the finite oscillation amplitude of the tip (peak-to-peak 1.7 Å in this case), by integrating $\partial F_z/\partial z$ over the oscillation [50].
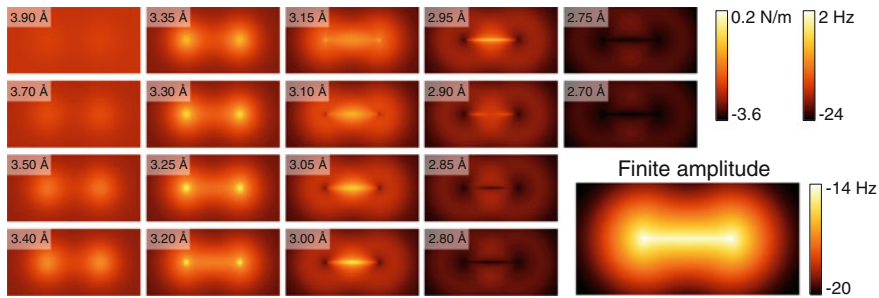
Fig. 10.8 Vertical force gradient ($\partial F_z / \partial z$) at different heights above the two atoms showing the evolution of the contrast at the low amplitude limit; all images with the *same color* scale ($k_{CO} = 0.6$ N/m). The finite amplitude image is calculated from the set assuming an oscillation amplitude ranging over the whole set, i.e. peak-to-peak amplitude $A_{p\text{-}p} = 1.2$ Å

Figure 10.8 shows the evolution of the force gradient as a function of tip height taking into account the tip relaxation. The series starts at a height of 3.9 Å, which is close to the equilibrium distance of the oxygen on the CO and the two carbon atoms on the surface. At this height, the CO does not bend considerably as the forces acting on it are rather weak. Once the tip is brought closer, the force gradient on top of the atoms begins to sharpen due to the CO bending away from the potential on top of the atoms. At around 3.1 Å, the contrast directly on top of the atoms abruptly changes. At this point the CO becomes unstable on top of the atoms. Even thought the lateral forces cancel out on top of the potential maxima, the gradient of the lateral forces eventually exceeds the lateral force constant of the tip and causes the inversion in contrast. Taking the tip even closer to the sample causes the saddle surface of the potential between the atoms to go through a similar evolution; first a sharpening and then eventually a contrast inversion. Finally at very close distances, the tip flexibility starts to dominate and $\partial F_z / \partial z$ starts to level off through-out the image.

However, neither the atoms nor the bonds appear dark when taking into account the full oscillation amplitude by integrating over the panels shown in Fig. 10.8. What happens though is that the relative intensity of the Δf signal on top of the atoms reduces. This causes the atoms and the saddle surface between them to appear almost equally bright and further strengthens the impression of visualizing bonds between the atoms as lines drawn in chemical diagrams.

The above model does not take into account the actual chemical bonds between the atoms in any way. In a covalent bond, the electron density is increased between the bound atoms leading to stronger Pauli repulsion of the CO apex on the bond. With regard to the tip model used here, this would not change the sharpening mechanism as it would just slightly increase the potential on the saddle surface between the bound atoms. The model however allows bond-like contrast to appear in AFM images with no actual bonds, provided that two atoms are close enough to one another to form a saddle surface in the potential between them.

This type of contrast has been observed in AFM images of various systems [6, 9, 18, 51]. In particular, intermolecular contrast has been interpreted as originating from hydrogen bonds, even though it is not clear why a mainly electrostatic interaction should give rise to repulsive contrast in AFM images. It is even possible to observe intermolecular contrast in a system where there is no underlying intermolecular bond [9, 18]. One example of a system where the flexibility of the CO causes bonds to be imaged where no bonds exist is formed by bis(para-pyridyl)acetylene (BPPA) molecules [18]. On an Au(111) substrate, the BPPA molecules form tetramers stabilized by hydrogen bonds between the pyridinic nitrogens and the hydrogens of the adjacent molecules. As a consequence of the hydrogen bonding (red dashed lines in Fig. 10.9b), two nitrogens are pushed close to one another. It is clear that the two nitrogens with their lone electron pairs do not form a bond with one another. The total electron density calculated by DFT in Fig. 10.9c also shows negligible electron density between the nitrogens. Yet, with small tip sample distances, bond-like contrast is observed both on the actual hydrogen bonds and and between the nitrogens.

The formation mechanism of the intermolecular contrast here is the same as in the case of the two atoms presented above and can be reproduced well using the same simple model. The evolution of the intermolecular contrast formation as a
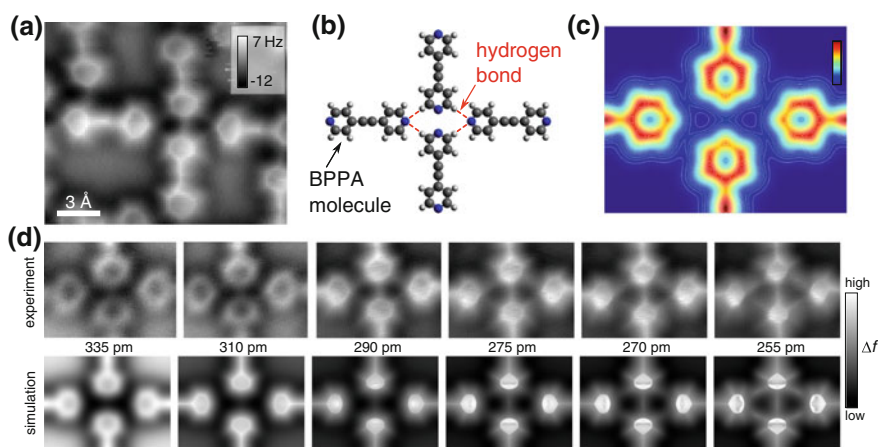

Fig. 10.9 Formation of intermolecular contrast between BPPA molecules. **a** Constant-height AFM image of a BPPA tetramer formed on gold. **b** Schematic representation of the tetramer with the *dashed red lines* marking the hydrogen bonds that stabilize the tetramer. **c** Total electron density given by DFT 3.1 Å above the molecular plane. **d** (*top row*) Experimental constant-height AFM images with a CO tip taken at different heights on top of the tetramer junction showing the appearance of both C–H$\cdots$N and N–N intermolecular contrast at close tip-sample distances. (*bottom row*) Simulated constant-height AFM images with a flexible CO tip ($k_{CO} = 0.6$ N/m) at the given heights showing the appearance of the same intermolecular contrast. The relative height scale is the same in the experimental and simulated images (simulated image at 385 pm matches the experimental image corresponding to the tunneling set-point of 0.1 V/10 pA). The heights correspond to the lowest point of the tip oscillation. Adapted with permission from [18]. Copyright (2014) by the American Physical Society

function of the tip height is shown in Fig. 10.9d. With large tip-sample distances, no intermolecular contrast appears either in simulation or in experiment. At these tip heights, the repulsion from the opposing nitrogens does not reach the middle point between them and no saddle surface is formed. Taking the tip closer, lines start to appear both between the two opposing nitrogens and on the actual hydrogen bonds holding the tetramer together. The contrast first appears between the two opposing nitrogens as they are closer to one another and hence the saddle surface is formed there first. On the hydrogen bonds the saddle surface only starts to appear when the tip reaches the repulsion from the hydrogen in the hydrogen bond.

The contrast saturation at small tip-sample distances demonstrated earlier with the two atoms also appears here. At the closest tip-sample distances, the contrast on the hydrogen bonds and between the nitrogens becomes indistinguishable from the contrast on the acetylene moieties, even though the electron density, and hence the repulsion, is much larger on the acetylene moieties. The reason is the same as in the case of the two atoms (Fig. 10.8). At the point when the CO becomes unstable on the saddle surface, the intensity of the Δf signal no longer increases there. This point is obviously first reached on the acetylene moiety, but eventually also on parts with the intermolecular contrast, rendering the magnitude of the Δf signal the same on both areas. Then, the contrast in the AFM images is dictated by the lateral stiffness of the CO and is no longer related to the magnitude of the tip-sample interaction.

10.5 Conclusions

We have discussed the effects of tip reactivity and flexibility and the role of background forces on the AFM response in molecular systems. Depending on the tip reactivity, it is possible to observe either only repulsive or attractive and repulsive atomic contrast. The apparent atomic positions are affected by the background signal from the neighbouring atoms as well as the possible flexibility of the tip apex.

Tip flexibility has other important consequences for AFM imaging in addition to causing shifts in the apparent atomic positions. The tip bends away from the ridges in the saddle surface of the tip-sample interaction potential, which produces sharp lines between nearby atoms. At the same time, the tip flexibility decreases the Δf signal directly on top of the atoms. These effects enhance the contrast on the bonds which makes it easier to recognize the molecular backbone in the AFM images. On the other hand, at sufficiently small tip-sample separations, the saddle surfaces in the tip-sample interaction potential surface and the atoms become equally bright, irrespective of the electron density of the sample. At this point the contrast formation in AFM is dictated by the lateral stiffness of the CO and is no longer related to the magnitude of the tip-sample interaction. This implies that intermolecular contrast does not directly correspond to the presence of an intermolecular bond. Consequently, quantitative understanding of intra- and intermolecular contrast in AFM images requires taking into account the effects from tip flexibility.

References

1. L. Gross, F. Mohn, N. Moll, P. Liljeroth, G. Meyer, Science **325**, 1110 (2009)
2. Y. Sugimoto, P. Pou, O. Custance, P. Jelínek, M. Abe, R. Perez et al., Science **322**, 413 (2008)
3. J. Welker, A.J. Weymouth, F.J. Giessibl, ACS Nano. **7**, 7377 (2013)
4. L. Gross, F. Mohn, N. Moll, B. Schuler, A. Criado, E. Guitián et al., Science **337**, 1326 (2012)
5. F. Mohn, L. Gross, N. Moll, G. Meyer, Nat. Nanotech. **7**, 227 (2012)
6. J. Zhang, P. Chen, B. Yuan, W. Ji, Z. Cheng, X. Qiu, Science **342**, 611 (2013)
7. L. Gross, F. Mohn, N. Moll, G. Meyer, R. Ebel, W.M. Abdel-Mageed et al., Nat. Chem. **2**, 821 (2010)
8. F. Mohn, J. Repp, L. Gross, G. Meyer, M. Dyer, M. Persson, Phys. Rev. Lett. **105**, 266102 (2010)
9. N. Pavliček, B. Fleury, M. Neu, J. Niedenführ, C. Herranz-Lancho, M. Ruben et al., Phys. Rev. Lett. **108**, 086101 (2012)
10. F. Albrecht, M. Neu, C. Quest, I. Swart, J. Repp, J. Am. Chem. Soc. **135**, 9200 (2013)
11. D.G. de Oteyza, P. Gorman, Y.C. Chen, S. Wickenburg, A. Riss, D.J. Mowbray et al., Science **340**, 1434 (2013)
12. A. Riss, S. Wickenburg, P. Gorman, L.Z. Tan, H.Z. Tsai, D.G. de Oteyza et al., Nano. Lett. **14**, 2251 (2014)
13. F. Mohn, B. Schuler, L. Gross, G. Meyer, Appl. Phys. Lett. **102**, 073109 (2013)
14. Z. Sun, M.P. Boneschanscher, I. Swart, D. Vanmaekelbergh, P. Liljeroth, Phys. Rev. Lett. **106**, 046104 (2011)
15. M.P. Boneschanscher, S.K. Hämäläinen, P. Liljeroth, I. Swart, ACS Nano. **8**, 3006 (2014)
16. M. Neu, N. Moll, L. Gross, G. Meyer, F.J. Giessibl, J. Repp, Phys. Rev. B **89**, 205407 (2014)
17. P. Hapala, G. Kichin, C. Wagner, F.S. Tautz, R. Temirov, P. Jelínek, Phys. Rev. B **90**, 085421 (2014)
18. S.K. Hämäläinen, N. van der Heijden, J. van der Lit, S. den Hartog, P. Liljeroth, I. Swart, Phys. Rev. Lett. **113**, 186102 (2014)
19. G.H. Enevoldsen, H.P. Pinto, A.S. Foster, M.C.R. Jensen, A. Kühnle, M. Reichling et al., Phys. Rev. B **78**, 045416 (2008)
20. P. Pou, S.A. Ghasemi, P. Jelínek, T. Lenosky, S. Goedecker, R. Perez, Nanotechnology **20**, 264015 (2009)
21. M. Ondráček, P. Pou, V. Rozsíval, C. González, P. Jelínek, R. Pérez, Phys. Rev. Lett. **106**, 176101 (2011)
22. J. Welker, F.J. Giessibl, Science **336**, 444 (2012)
23. A. Yurtsever, D. Fernández-Torre, C. González, P. Jelínek, P. Pou, Y. Sugimoto et al., Phys. Rev. B **85**, 125416 (2012)
24. M.P. Boneschanscher, J. van der Lit, Z. Sun, I. Swart, P. Liljeroth, D. Vanmaekelbergh, ACS Nano. **6**, 10216 (2012)
25. M. Schneiderbauer, M. Emmrich, A.J. Weymouth, F.J. Giessibl, Phys. Rev. Lett. **112**, 166102 (2014)
26. D.M. Eigler, C.P. Lutz, W.E. Rudge, Nature **352**, 600 (1991)
27. L. Bartels, G. Meyer, K.H. Rieder, Appl. Phys. Lett. **71**, 213 (1997)

28. S. Loth, K. von Bergmann, M. Ternes, A.F. Otte, C.P. Lutz, A.J. Heinrich, Nat. Phys. **6**, 340 (2010)
29. F.J. Giessibl, Appl. Phys. Lett. **73**, 3956 (1998)
30. P.R. Wallace, Phys. Rev. **71**, 622 (1947)
31. A.H. Castro Neto, F. Guinea, N.M.R. Peres, K.S. Novoselov, A.K. Geim, Rev. Mod. Phys. **81**, 109 (2009)
32. J. Coraux, A.T. N'Diaye, C. Busse, T. Michely. Nano. Lett. **8**, 565 (2008)
33. I. Pletikosić, M. Kralj, P. Pervan, R. Brako, J. Coraux, A.T. N'Diaye et al., Phys. Rev. Lett. **102**, 056808 (2009)
34. J. Coraux, T.N. Plasa, C. Busse, T. Michely, New J. Phys. **10**, 043033 (2008)
35. S.K. Hämäläinen, M.P. Boneschanscher, P.H. Jacobse, I. Swart, K. Pussi, W. Moritz et al., Phys. Rev. B **88**, 201406 (2013)
36. J.E. Sader, S.P. Jarvis, Appl. Phys. Lett. **84**, 1801 (2004)
37. P.J. Feibelman, Phys. Rev. B **77**, 165419 (2008)
38. J. van der Lit, M.P. Boneschanscher, D. Vanmaekelbergh, M. Ijäs, A. Uppstu, M. Ervasti et al., Nat. Commun. **4**, 2023 (2013)
39. Z. Yang, M. Corso, R. Robles, C. Lotze, R. Fitzner, E. Mena-Osteritz et al., ACS Nano. **8**, 10715 (2014)
40. G.M. Rutter, J.N. Crain, N.P. Guisinger, T. Li, P.N. First, J.A. Stroscio, Science **317**, 219 (2007)
41. M. Ijäs, M. Ervasti, A. Uppstu, P. Liljeroth, J. van der Lit, I. Swart et al., Phys. Rev. B **88**, 075429 (2013)
42. E. Cockayne, G.M. Rutter, N.P. Guisinger, J.N. Crain, P.N. First, J.A. Stroscio, Phys. Rev. B **83**, 195425 (2011)
43. J. Cai, P. Ruffieux, R. Jaafar, M. Bieri, T. Braun, S. Blankenburg et al., Nature **466**, 470 (2010)
44. L. Yang, C.H. Park, Y.W. Son, M.L. Cohen, S.G. Louie, Phys. Rev. Lett. **99**, 186801 (2007)
45. Y.W. Son, M.L. Cohen, S.G. Louie, Nature **444**, 347 (2006)
46. A. Rycerz, J. Tworzydlo, C.W.J. Beenakker, Nat. Phys. **3**, 172 (2007)
47. M. Koch, F. Ample, C. Joachim, L. Grill, Nat. Nanotech. **7**, 713 (2012)
48. B. Schuler, W. Liu, A. Tkatchenko, N. Moll, G. Meyer, A. Mistry et al., Phys. Rev. Lett. **111**, 106103 (2013)
49. N. Moll, L. Gross, F. Mohn, A. Curioni, G. Meyer, New J. Phys. **12**, 125020 (2010)
50. F.J. Giessibl, Appl. Phys. Lett. **78**, 123 (2001)
51. A.M. Sweetman, S.P. Jarvis, H. Sang, I. Lekkas, P. Rahe, Y. Wang et al., Nat. Commun. **5**, 3931 (2014)